

# 3D Impedance Modelling of Metal Anodes in Solid-State Batteries – Incompatibility of Pore Formation and Constriction Effect in Physical-Based 1D Circuit Models

Janis K. Eckhardt<sup>1,2\*</sup>, Till Fuchs<sup>2,3</sup>, Simon Burkhardt<sup>2,3</sup>, Peter J. Klar<sup>2,4</sup>, Jürgen Janek<sup>2,3</sup>, and Christian Heiliger<sup>1,2</sup>

<sup>1</sup>Institute for Theoretical Physics, Justus Liebig University,  
Heinrich-Buff-Ring 16, D-35392 Giessen, Germany.

<sup>2</sup>Center for Materials Research (ZfM), Justus Liebig University,  
Heinrich-Buff-Ring 16, D-35392 Giessen, Germany.

<sup>3</sup>Institute of Physical Chemistry, Justus Liebig University,  
Heinrich-Buff-Ring 17, D-35392 Giessen, Germany.

<sup>4</sup>Institute of Experimental Physics I, Justus Liebig University,  
Heinrich-Buff-Ring 16, D-35392 Giessen, Germany.

\*janis.k.eckhardt@theo.physik.uni-giessen.de

This document is the Accepted Manuscript version of a Published Work that appeared in final form in ACS Applied Materials & Interfaces, copyright © 2022 The Authors. Published by American Chemical Society after peer review and technical editing by the publisher. To access the final edited and published work see <https://doi.org/10.1021/acsami.2c12991>.

## Abstract

A non-ideal contact at the electrode/solid electrolyte interface of a solid-state battery arising due to pores (voids) or inclusions results in a constriction effect that severely deteriorates the electric transport properties of the battery cell. The lack of understanding of this phenomenon hinders the optimization process of novel components, such as reversible and high-rate metal anodes. Deeper insight into the constriction phenomenon is necessary to correctly monitor interface degradation and to accelerate the successful use of metal anodes in solid-state batteries. Here, we use a 3D electric network model to study the fundamentals of the constriction effect. Our findings suggest that dynamic constriction as a non-local effect cannot be captured by conventional 1D equivalent circuit models and that its electric behavior is not ad hoc predictable. It strongly depends on the interplay of the geometry of the interface causing the constriction and the microscopic transport processes in the adjacent phases. In the presence of constriction, the contribution from the non-ideal (porous) electrode/solid electrolyte interface to the impedance spectrum may exhibit two signals that cannot be explained when the porous interface is described by a physical-based (effective medium theory) 1D equivalent circuit model. In consequence, the widespread assumption of a single interface contribution to the experimental impedance spectrum may be entirely misleading and can cause serious misinterpretation.

## Introduction

Particularly in solid-state batteries (SSB), establishing and maintaining full electric contact between individual phases and components presents a severe challenge in addition to the chemical stability of the interfaces involved.<sup>1-4</sup> Pores naturally form during the mechanical assembly of the battery cell's layered architecture or may even form at interfaces under operation (e.g., during electrode stripping/dissolution at reversible metal anodes). Pore formation reduces the electrochemically active surface area and thus severely affects the electric transport properties of the cell.<sup>5-8</sup> Porous interfaces between a metal electrode and a solid electrolyte (SE) are often studied as a function of applied uniaxial pressure as the application of uniaxial pressure to the battery cell is a key process step during assembly of the different layers of solid-state batteries. Systematically increasing the applied pressure allows to continuously tune the pore density and distribution and, thus, the interface morphology and effective contact area.<sup>9</sup> While high pressure may be well used during formation of a battery cell to optimize the local microstructure, stack pressure during later battery operation should be low (in the order of about 1 MPa or lower) in order to meet the requirements for battery packs.

Impedance spectroscopy (IS), as a non-destructive method, is particularly suited for systematically studying the kinetics of solid/solid interfaces. When the frequency  $f$  of the exciting electric field in the IS measurement is swept over a wide range, different transport processes contributing to the overall electric response of the sample probed may be separated from each other, if their characteristic frequencies differ. IS data are usually analyzed by means of macroscopic (physical-based) 1D-equivalent circuit models, assuming that each component of the equivalent circuit represents a transport process at the microscopic level. Microstructural information, however, is typically not considered in the analysis, although it can have a major impact on the impedance, leading to further challenges in the interpretation of experimental data as will be demonstrated in this study.<sup>10</sup>

In case of a reversible metal anode, the experimental system typically consists of a polycrystalline and cation-conducting solid electrolyte that is in contact with an alkali metal working electrode (WE), e.g. lithium metal in contact with a garnet-type SE such as variants of  $\text{Li}_7\text{La}_3\text{Zr}_2\text{O}_{12}$  (LLZO) or sodium metal in contact with a NASICON-type SE such as  $\text{Na}_{3.4}\text{Zr}_2\text{Si}_{2.4}\text{P}_{0.6}\text{O}_{12}$ .<sup>11-18</sup> Usually, one would account for four different electric migration processes on the microscopic level, i.e., electronic transport in the metal electrode, electric charge transfer (CT) at the electrode/SE interface, and bulk as well as grain boundary (GB) ionic transport within the SE. Remaining pores at a non-ideal interface, surrounded by the metal WE on one side and the SE on another side, act as local capacitors. At varying voltage (e.g., in an IS measurement), their impedance strongly depends on the frequency  $f$  of the external electric field. At constant voltage (DC electric field,  $f = 0$  Hz), the pores possess an infinitely large impedance. Thus, the active contact area between WE and SE is reduced by the pores, leading to (dynamic) current constriction at the interface. In our previous paper, we analyzed the constriction effect for a rather simple model case, i.e. pores on a homogeneous SE with zero polarization resistance.<sup>19</sup> Earlier work already considered this type of individual single crystal contacts, which is sufficient to study the origin of the constriction effect as such.<sup>20-25</sup> The equipotential lines in the SE region below the contact areas are not parallel to the interface as a consequence of current spreading within the SE. At high frequencies of the external electric field (AC,  $f \rightarrow \infty$  Hz), the impedance of the pore even approaches zero and a high displacement current will flow, starting from the entire electrode. The resulting dynamic constriction effect cannot be considered as a local

microscopic effect as it is determined by the morphology of the interface at least on a mesoscopic scale of nanometers to micrometers and can affect an almost macroscopic region below the contact.

However, the situation is more complicated in case of (realistic) non-ideal contacts between a metal WE and a ceramic, polycrystalline SE exhibiting an inhomogeneous interface morphology. The reason is that the impact of the dynamic constriction effect on the electric properties of such an interface is far from local. The depth of the *constriction region*, i.e., the region where the equipotential lines are not parallel to the otherwise planar interface, varies with the frequency  $f$  of the externally applied electric field.<sup>19-25</sup> As a consequence, the constriction phenomenon also affects the macroscopic impedance response of the SE, i.e., the latter is not solely determined by the microscopic transport processes within the grains and across GBs.

In this study, we extend our previous approach and use a 3D electric network model to compute impedance data of realistic 3D model systems. The computational results are treated like experimental data in the standard impedance analysis procedure to illustrate the challenges and loss of information that occur when using 1D circuit models. We show that the interface impedance is determined by two contributions, that of the CT across the physical contact and that of the (dynamic) constriction effect. As both contributions generally exhibit a different frequency dependence, their interplay may yield one or two distinct semicircles in the Nyquist representation of the impedance spectrum. An analysis of the constriction effect with physical-based 1D circuit models is not straightforward as such models cannot fully capture the effects of frequency-dependent (3D) current spreading caused by dynamic constriction. As a consequence, the usually successful approach of correlating macroscopic components of physical-based 1D equivalent circuit models with single microscopic transport processes fails. Additional degrees of freedom are necessary to describe the constriction phenomenon in 1D fit circuit models. Their dependencies on the real 3D system (e.g., the microscopic transport quantities of the SE or the interface) are discussed.

## Computational Details

### 1. Description of Model Structure

As described in the introduction, metal anode interfaces in SSB often suffer from local contact loss for several reasons. To study interface effects between a reversible metal anode and a SE in a SSB cell, it is therefore often sufficient to solely consider a model system consisting of a (porous) metal working electrode (WE), a ceramic SE and an ideal metal counter electrode (CE). The latter serves as a quasi-reference electrode (QRE) as it provides a stable, invariant and ideal contact to the SE ( $A_{\text{electrode}} = A_{\text{contact}}$ ). Then, the impedance of the cell is dominated by the WE/SE interface, together with the properties of the bulk SE between the electrodes.<sup>15</sup> This avoids the use of traditional reference electrodes and the superposition of additional effects in the measurement. Figure 1 a) shows a 2D projection of a segment of such a 3D model structure in the vicinity of the WE/SE interface as it may be typically observed. The SE possesses a polycrystalline structure and pores (voids) at the WE/SE interface cause complex three-phase morphologies (metal, SE, pore space), making a systematic analysis of individual parameters challenging. Therefore, we deliberately simplify this system for studying the interplay between non-local current constriction and microscopic transport processes.

Without loss of generality, the number of geometric model parameters is reduced by increasing the symmetry of the system, e.g., for describing the microstructure of the SE or the interface morphology

(see Figure 1 b)). Note that the interface morphology affects the magnitude of individual geometric impedance parameters (e.g., constriction resistance) quantitatively, but not qualitatively, as already discussed in the literature.<sup>19,22</sup> Here, all contact spots are combined to a single squared contact of area  $A_{\text{contact}}$  in the center of the interface. The parallel gap of width  $\delta_{\text{Int}}$  between WE and SE outside the contact mimics the pore system. The microstructure of the polycrystalline SE is rearranged into a stack of planar GBs separated by bulk-like SE layers with a spacing of  $1/50 L_z$ , where  $L_z$  is the total thickness of the SE. The planar arrangement enables a straightforward translation of the model structure into a 1D equivalent circuit. Moreover, the WE, CE and the SE are assumed to be of the same area ( $A_{\text{SE}} = L_x \cdot L_y$ ).

Despite these simplifications, the 3D computational model structure pertains the key features of the real solid electrolyte, but it is less complex. It still grabs important properties of the dynamic constriction effect, i.e., current spreading, curved equipotential lines, and frequency-dependent volume changes of the constriction region. This facilitates a systematic analysis of the impact of individual material parameters on the impedance.

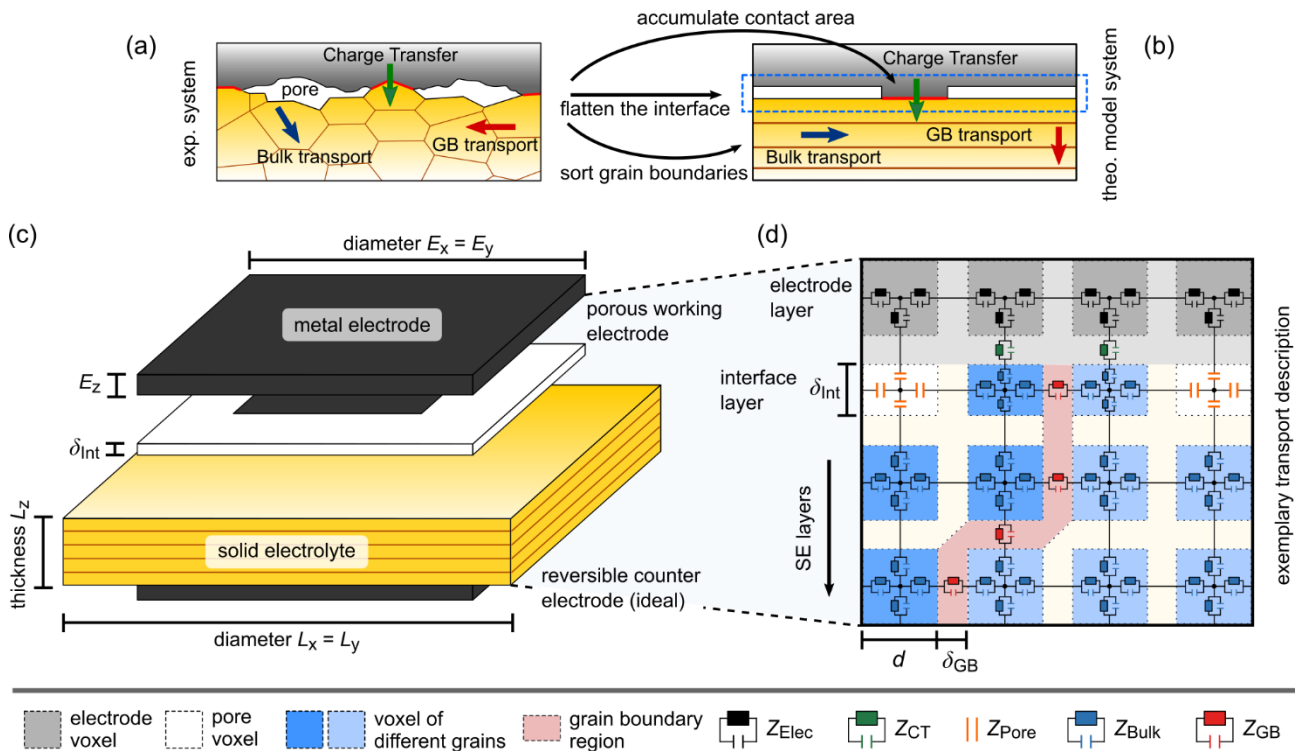


Figure 1. Overview of the computational model. (a) – (b) The real system is transformed into a simplified theoretical model system to enable systematic studies of individual model parameters. (c) The potential is applied between the porous working electrode (non-ideal) and the reversible counter electrode (ideal). Changes in the contact between working electrode and polycrystalline SE are described by the interface layer. (d) Charge transport processes are described by different RC-elements in the 3D electric network, while the pores at the interface are considered as capacitors.

## 2. Description of the 3D Impedance Network

A 3D impedance network model is used for the computation of impedance spectra  $Z(f)$  of our model system depicted in Figure 1 b). First, the structure is divided into individual voxels of edge length  $d$  that are assigned to either a grain within the SE (bluish), a pore at the WE/SE interface (white) or one

of the metal electrodes (grey). The non-ideal interface morphology is modeled by a separate layer of voxels of constant thickness  $\delta_{\text{Int}}$  that reflects the contact between WE and SE (see Figure 1 c)).

The transport processes at the microscopic level, i.e., between individual voxels of the discretized structure, are described by different local equivalent circuit elements, as depicted in Figure 1 d). While bulk transport and transport across GBs within the SE as well as the CT step at the electrode/SE interface are considered by different  $RC$ -elements ( $Z_{\text{Bulk}}$ ,  $Z_{\text{Elec}}$ ,  $Z_{\text{GB}}$ ,  $Z_{\text{CT}}$ ), the pores at the interface are solely described as capacitors ( $Z_{\text{Pore}}$ ). Microscopic bulk and GB transport are modeled by two ( $2 \cdot Z_{\text{Bulk}}$ ) and three ( $2 \cdot Z_{\text{Bulk}} + Z_{\text{GB}}$ )  $RC$ -elements connected in series, respectively. The transport within the metal electrode is described by ( $2 \cdot Z_{\text{Elec}}$ ) and the CT step at both interface by ( $Z_{\text{Elec}} + Z_{\text{CT}} + Z_{\text{Bulk}}$ ). Pore transport is considered either by the series connection of an  $RC$ -element with a capacitor ( $Z_{\text{Elec}} + Z_{\text{Pore}}$ , or  $Z_{\text{Bulk}} + Z_{\text{Pore}}$ ) or by two capacitors ( $2 \cdot Z_{\text{Pore}}$ ) connected in series, depending on the structural properties of the voxels involved. The local parameters ( $R_{i, \text{loc}}$ ,  $C_{i, \text{loc}}$ ) of the bulk, GB and pore circuit elements are calculated according to the rules for conductors and plate capacitors based on conductivities  $\sigma_i$  and permittivities  $\epsilon_i$ . In contrast, the parameters of the local  $R_{\text{CT}}C_{\text{CT}}$ -element result from the polarization resistance  $R_{\text{Pol}}$  and the double-layer capacitance  $C_{\text{DL}}$  at the interface. Further details about setting up and solving the electric network model as well as computing an impedance spectrum are given in our previous work.<sup>10</sup>

### 3. Computational Parameters and Analysis of the Impedance Spectra

A cubic shape of the SE ( $L_x = L_y = L_z$ ) corresponding to  $(50 \mu\text{m})^3$  and a GB thickness of 10 nm (core region and adjacent space-charge region) is assumed. The results described in what follows, however, also apply to larger system sizes up to several millimeters or even larger. Table 1 summarizes the parameters of the geometric model and the transport quantities used in the computations (cf. computational results in Figure 2 to Figure 7). All microscopic transport parameters are in the range of, but not limited to, those of the solid electrolyte LLZO.<sup>15</sup> The transport within the (metal) electrode is assumed to be resistance-free. The pore depth  $\delta_{\text{Int}}$  is given as a fraction of the transport length  $L_z$  and its value varies between the individual studies. In each series of impedance computations, the (relative) contact area  $A_{\text{contact}}/A_{\text{SE}}$  of the single square-shaped contact spot is systematically varied in size from 100 % (ideal contact, no pores) to 0 % (no contact, capacitor-like arrangement of WE and SE).

The analysis of the computed impedance spectra derived by the 3D electric network model is based on a simplified 1D “*fit model circuit*” consisting of a resistor connected in series with four  $RC$ -elements as depicted as inset in Figure 2 a). The fitting was carried out using the commercial software RelaxIS 3 (version 3.0.18.15, rhd instruments GmbH & Co. KG). The Kramers-Kronig test of the impedances computed by the 3D electric network model yields residuals in the order of  $10^{-6}$  %.<sup>26</sup> Thus, the computed impedances are (almost) free of noise signals, and it is valid to consider all data records ( $f$ ,  $Z$ ) in the 1D analysis approach.<sup>27</sup>

Note that individual transport parameters in the computations may be chosen to vary in a wider range than expected in experiment. This is related to our approach of exclusively changing the contact area (at constant pore depth  $\delta_{\text{Int}}$ ) throughout a computed impedance series ( $0 \% < A_{\text{contact}} \leq 100 \%$ ), which leads to an overestimation of  $\Delta\tau_{\text{Cstr}}$ , since both parameters have an opposite influence on  $\tau_{\text{Cstr}}$ .<sup>19</sup> The aim of our study is, among others, the understanding of the time constant’s  $\tau_{\text{Cstr}}$  impact on the

impedance spectrum and the derived macroscopic transport parameters. For this purpose, we discuss limiting cases distinguished by the arrangement of the time constants involved, i.e.,  $\tau_{\text{Bulk}}$ ,  $\tau_{\text{GB}}$ ,  $\tau_{\text{CT}}$ , and  $\tau_{\text{Cstr}}$ . To ensure that a specific order of time constants is preserved during a computational series, we sometimes artificially lower or increase individual time constants  $\tau_i$  by choosing “unrealistic” material parameters. For example, we modified the pore capacitance  $\tilde{C}_{\text{Pore}}$  in case of the constriction signal or the permittivity  $\epsilon_{\text{GB}}$  in case of the GB signal. However, this does not affect the qualitative results in these studies as the capacitance  $\tilde{C}_{\text{Pore}}$  influences exclusively the constriction impedance. Similarly, the permittivity  $\epsilon_{\text{GB}}$  and double layer capacitance  $C_{\text{DL}}$  only affect the corresponding macroscopic transport contributions and not that of geometric constriction.

Table 1: Overview of the transport parameters used in the computations. These are in the range of, but not limited to, those of the solid electrolyte LLZO. The bulk conductivity and permittivity were fixed to  $\sigma_{\text{Bulk}} = 0.46 \text{ mS/cm}$  and  $\epsilon_{\text{Bulk}} = 150 \cdot \epsilon_0$ , respectively.<sup>15, 28-29</sup> The GB thickness (core region and adjacent space-charge region) is set to  $\delta_{\text{GB}} = 10 \text{ nm}$ .<sup>15, 30</sup>

figure	$L_z/\delta_{\text{Int}}$	$\sigma_{\text{GB}} / \mu\text{S/cm}$	$R_{\text{Pol}} / \Omega \cdot \text{cm}^2$	$\epsilon_{\text{GB}} / \epsilon_0$	$\tilde{C}_{\text{Pore}} / \mu\text{F/cm}^2$	$C_{\text{DL}} / \mu\text{F/cm}^2$
2	50 k	5.97	1	150	8.85	885
3 (a)	50 k	5.97	-	150	88.5	-
3 (b)	50 k	5.97	-	1.5 M	0.89	-
4	50 k	variable	-	150	88.5	-
5 (a)	50 k	-	1	-	0.89	88.5
5 (b)	50 k	-	1	-	885	88.5
6	50 k	-	variable	-	885	8.85
7	50 k	-	10	-	885	8.85

## Results

### 1. Grabbing Non-Locality of Current Constriction in 1D Equivalent Circuit Modelling

The fundamentals of current constriction and its dependence on the interfacial morphology (e.g., pore depth or distribution of the contact area) have already been discussed in detail in our previous work<sup>19</sup> and also in early studies by Maier and Fleig.<sup>20-25</sup> Here, we compare the results of two different 1D equivalent circuit models with the impedance  $Z(f)$  of our 3D model structure (see Figure 1 b)) derived by the electric network model. The results help to underline the non-locality of dynamic constriction and its consequences. In what follows, the impedance  $Z(f)$  derived by the electric network model takes the place of a measured impedance spectrum and serves as input for 1D modelling approaches, commonly used for analyzing experimental impedance data. This helps to understand the loss of information, when “real” experimental data are analyzed only within a 1D impedance circuit model.

Figure 2 b) shows the potential distribution in the central cross section of the 3D model structure for various frequencies  $f$  of an applied electric AC field. The evolution of the potential distribution with  $f$  illustrates the key features of dynamic current constriction as a non-local effect, i.e., the effect of spatial focusing of the current paths at the contact spot and the corresponding bending of the equipotential lines. These are a consequence of the capacitor structure surrounding the contact area at the WE/SE interface. The capacitor structure has an infinitely large resistance in the DC case ( $f =$

0 Hz) and becomes highly conductive in case of large modulation frequencies  $f$  of the AC field. Thus, the depth of the constriction region where the current paths are not parallel to each other and the equipotential lines are not parallel to the interface varies. As a result, the impact of the constriction effect is not local, but affects several layers of the macroscopic sample structure. This was already pointed out by Maier and Fleig in their work.<sup>20-25</sup>

The inset in Figure 2 c) shows an intuitive and straightforward translation of the 3D model structure into a physical-based 1D equivalent circuit model. For the sake of clarity, we assume a reversible and resistance-free CE. The model is referred to as “*physical model*” (1D-PM) in the following. It can be described by four building blocks connected in series. The first building block  $Z_{\text{Elec}}^{\text{1D-PM}} = R_{\text{Elec}}$  describes the transport within the metal electrodes as purely ohmic, i.e.,  $C_{\text{Elec}}^{\text{1D-PM}} = 0$ . The second  $Z_{\text{Bulk}}^{\text{1D-PM}}$  and third  $Z_{\text{GB}}^{\text{1D-PM}}$  building blocks are modeled as  $RC$ -elements, respectively. They represent the microscopic transport processes within the grains and across GBs in the SE.<sup>31-33</sup> The fourth element describes the non-ideal WE/SE interface as a parallel connection of the capacitance of the pore  $C_{\text{Pore}}^{\text{1D-PM}}$  and an  $R_{\text{CT}}^{\text{1D-PM}}C_{\text{CT}}^{\text{1D-PM}}$ -element representing the CT at the physical contact. The interface description can be transformed into a single  $RC$ -element  $Z_{\text{interface}}^{\text{1D-PM}}$  only where the capacitor  $C_{\text{interface}}^{\text{1D-PM}}$  is the sum of the capacities  $C_{\text{CT}}^{\text{1D-PM}}$  and  $C_{\text{Pore}}^{\text{1D-PM}}$ . The three quantities  $C_{\text{Pore}}^{\text{1D-PM}}$ ,  $R_{\text{CT}}^{\text{1D-PM}}$ , and  $C_{\text{CT}}^{\text{1D-PM}}$  are derived by weighting with the corresponding contact areas.

$$R_{\text{interface}}^{\text{1D-PM}} = R_{\text{CT}}^{\text{1D-PM}} = R_{\text{Pol}} \cdot A_{\text{contact}} \quad (1)$$

$$C_{\text{interface}}^{\text{1D-PM}} = C_{\text{CT}}^{\text{1D-PM}} + C_{\text{Pore}}^{\text{1D-PM}} = C_{\text{DL}} \cdot A_{\text{contact}} + \tilde{C}_{\text{Pore}} \cdot (1 - A_{\text{contact}}) \quad (2)$$

As a result, the 1D-PM can be represented as one resistor  $Z_{\text{Elec}}^{\text{1D-PM}}$  plus three  $RC$ -elements  $Z_{\text{interface}}^{\text{1D-PM}}$ ,  $Z_{\text{Bulk}}^{\text{1D-PM}}$ , and  $Z_{\text{GB}}^{\text{1D-PM}}$  in a serial configuration.

Figure 2 a) and c) show a series of impedance spectra in Nyquist representation for different contact areas  $A_{\text{contact}}$  computed by the 3D network model based on the realistic sample structure on the one hand and calculated or predicted by the 1D-PM on the other hand. The underlying microscopic transport parameters used in both sets of computations are the same and given in Table 1. The impedance series of the 1D-PM consist of three semicircles corresponding to the frequency-dependent signals of  $Z_{\text{Bulk}}^{\text{1D-PM}}$  (blue),  $Z_{\text{GB}}^{\text{1D-PM}}$  (red), and  $Z_{\text{interface}}^{\text{1D-PM}}$  (light green). The comparison with the 3D network model computations, however, reveals some significant discrepancies. In particular, the 1D-PM cannot grasp the evolution of a fourth (dynamic constriction) contribution to the impedance of the model system (yellow), which increases with decreasing contact area.

Since the 1D physical (prediction) model fails in fully describing the realistic 3D model system, we define a “*fit model*” (1D-FM) circuit depicted in the inset of Figure 2 a). It is a serial connection of five circuit elements and, thus, exhibits more degrees of freedom than the original (physical) 1D-PM. Again, we assume a resistance  $Z_{\text{Elec}}^{\text{1D-FM}} = R_{\text{Elec}}$  for the transport within the metal WE and  $RC$ -elements  $Z_{\text{Bulk}}^{\text{1D-FM}}$  and  $Z_{\text{GB}}^{\text{1D-FM}}$  for describing the transport within the SE. The non-ideal WE/SE interface is now described by two independent  $RC$ -elements in series resulting from charge transfer  $Z_{\text{CT}}^{\text{1D-FM}}$  and dynamic constriction  $Z_{\text{Cstr}}^{\text{1D-FM}}$ .

It turns out that this model with its four semicircles possesses enough degrees of freedom for adequately fitting all impedance spectra derived with the 3D network model for the highly symmetric model system. However, the interpretation of the 1D model parameters ( $R_i$ ,  $C_i$ ), in particular for  $i =$  (CT or Cstr), derived by fitting the 3D computations is not straightforward, as the independent

treatment of charge transfer and dynamic constriction at the interface in 1D-FM is not intuitive. This becomes apparent when comparing the predictions of the 1D-PM with the 3D network model results and its derived macroscopic transport quantities ( $R_i$ ,  $C_i$ ) based on fitting with the 1D-FM. While the contributions corresponding to bulk and GB transport within the SE are similar, i.e.,  $Z_{\text{Bulk}}^{\text{1D-FM}} \approx Z_{\text{Bulk}}^{\text{1D-PM}}$  and  $Z_{\text{GB}}^{\text{1D-FM}} \approx Z_{\text{GB}}^{\text{1D-PM}}$ , this does not hold for the parameters of the interface.

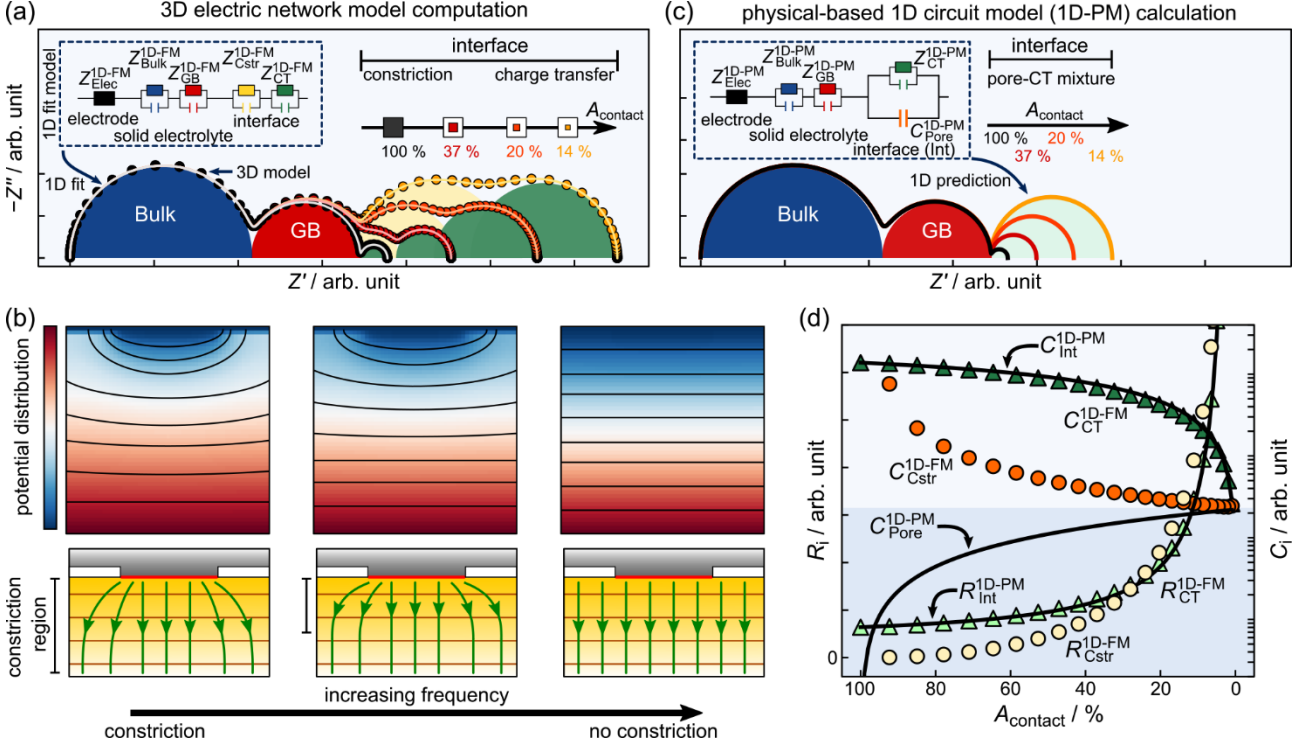


Figure 2. *Non-local dynamic constriction effect and failure of the physical-based 1D equivalent circuit model in describing it. (a) Series of impedance spectra computed with the 3D electric network model (dots). A fourth (constriction) semicircle (yellow) arises resulting from the WE/SE interface, when the contact area is reduced ( $A_{\text{electrode}} > A_{\text{contact}}$ ). (b) Potential distributions and current lines for three different excitation frequencies highlight the effect of dynamic constriction, i.e., frequency-dependent change of the active electrode area and variations in the size of the constriction region. (c) Transfer of the 3D model system depicted in Figure 1 b) into a physical-based 1D equivalent circuit (inset). Corresponding impedance spectra calculated or predicted for different contact areas  $A_{\text{contact}}$  between WE and SE using the same parameters reveal three semicircles only. Constriction cannot be captured by the 1D-PM, but it can be fitted using the 1D-FM (inset in (a)). (d) Comparison of the predictions by the 1D-PM (solid lines) with the derived parameters ( $R_i$ ,  $C_i$ ) of the interface (circular and triangle symbols) based on the 1D fitting approach of the 3D network model computations.*

Figure 2 d) shows the constriction parameters  $R_{\text{Cstr}}^{\text{1D-FM}}$  and  $C_{\text{Cstr}}^{\text{1D-FM}}$  as circular symbols, that of the charge transfer  $R_{\text{CT}}^{\text{1D-FM}}$  and  $C_{\text{CT}}^{\text{1D-FM}}$  as triangular symbols and the 1D-PM predictions calculated according to Equations (1) to (2) as solid lines. The qualitative behavior of  $R_{\text{CT}}^{\text{1D-FM}}$  and  $R_{\text{Cstr}}^{\text{1D-FM}}$  is very similar and their dependence on  $A_{\text{contact}}$  resembles that of  $R_{\text{Int}}^{\text{1D-PM}}$ , i.e., in case of  $R_{\text{CT}}^{\text{1D-FM}}$  it even matches that of  $R_{\text{Int}}^{\text{1D-PM}}$ . The trends of the two capacitances  $C_{\text{CT}}^{\text{1D-FM}}$  and  $C_{\text{Cstr}}^{\text{1D-FM}}$  as a function of  $A_{\text{contact}}$  differ significantly in values and curvature. The behavior of  $C_{\text{CT}}^{\text{1D-FM}}$  agrees with  $C_{\text{Int}}^{\text{1D-PM}}$ , but none of the fitted capacitances agree with  $C_{\text{Pore}}^{\text{1D-PM}}$  as a function of  $A_{\text{contact}}$ . Thus, only the functional dependence

of  $R_{CT}^{1D-FM}$  and approximately that of  $C_{CT}^{1D-FM}$  follow the dependence on contact area given by 1D-PM. Note that the predicted functional behavior is not universal, it depends on the order of the involved characteristic time constants as will be discussed in the next section.

Only in the limiting case where  $Z_{Cstr}^{1D-FM}$  is zero, i.e.,  $A_{contact} = A_{SE}$ , the impedance computed with the 3D electric network model is identical to that of the 1D-PM. The treatment of dynamic constriction and CT effect in 1D-FM as independent  $RC$ -elements leads to relaxation times  $\tau_{Cstr}^{1D-FM} = (R_{Cstr}^{1D-FM} \cdot C_{Cstr}^{1D-FM})$  and  $\tau_{CT}^{1D-FM} = (R_{CT}^{1D-FM} \cdot C_{CT}^{1D-FM})$  that depend on the contact area. Their time response, however, does not follow the prediction of the 1D-PM which describes the effect of the porous interface solely as a local effect. Therefore, dynamic constriction cannot be correlated with a local electric migration process in the system, as usually done in macroscopic physical-based 1D equivalent circuit models. Consequently, the underlying assumption that every contribution in the impedance corresponds to a microscopic electric migration process in the system does not hold.<sup>10, 34</sup>

## 2. Dependence of the Constriction Characteristics on other Sample Parameters

We will now discuss how the non-locality and the frequency dependence of the dynamic constriction effect influences the impedance response. The focus is on the SE, its microstructure and the microscopic transport processes inside, and also on the electrode/SE interfacial properties. For this purpose, we compute series of impedance spectra based on the 3D model structure depicted in Figure 1 b). Throughout such a series, specific model parameters are varied systematically, e.g., contact area or the materials parameters. All impedance spectra were subsequently fitted based on the 1D-FM. The corresponding macroscopic transport quantities ( $R_i^{1D-FM}$ ,  $C_i^{1D-FM}$ ) and the characteristic time constants  $\tau_i^{1D-FM}$  assigned to the various transport processes are then analyzed. We will omit the superscript “1D-FM” for all these transport quantities in the remainder of this section.

To ensure in the following that the computational results on the interplay of dynamic constriction with microscopic transport processes are comprehensible, the origin of the corresponding time constants  $\tau_i = R_i \cdot C_i$  (or characteristic frequencies  $\omega_i = 1/\tau_i$ ) has to be clarified first. A microscopic electric migration process is usually described by an  $RC$ -element in a macroscopic 1D circuit model. At its characteristic frequency, the conduction response of the transport process changes from electric to dielectric (rule of thumb) with increasing frequency  $f$  of the exciting external electric field. Although dynamic constriction can also be described by an  $RC$ -element in a macroscopic 1D fit circuit model, it is not directly related to a microscopic electric migration process. Its time constant  $\tau_{Cstr}$  corresponds to a characteristic frequency below which pores at the interface are electrically insulating and above which the pores are dielectrically conductive. This frequency-dependent switching of the active contact area  $A_{electrode, active}$  opens up additional transport paths through the SE for externally applied frequencies above  $1/\tau_{Cstr}$  (cf. Figure 2 b)). These additional transport paths influence the macroscopic transport parameters ( $R_i$ ,  $C_i$ ) derived from fitting the impedance spectra and may also affect the relaxation times deduced for other transport processes. This “switching” of apparently electrically inactive pore areas from insulating to dielectrically conducting as the key ingredient of the constriction effect, has so far been mostly overlooked in the literature.

## 2.1 Effects of the Solid Electrolyte Characteristics on the Constriction Effect

First, we will solely focus on the interplay of the SE properties and the constriction effect. We assume that the CT step at both electrode/SE interfaces is resistance-free for the sake of simplicity and without loss of generality. We start considering the effect of the order of the time scales on the macroscopic transport characteristics ( $R_i$ ,  $C_i$ ) of the SE ( $i = \text{Bulk}$  and  $\text{GB}$ ) derived by the 1D fitting approach and then discuss the effects of different microscopic transport parameters ( $\sigma_i$ ,  $\varepsilon_i$ ) of the SE on the constriction parameters. The latter is related to the fact that constriction as a geometric effect is relevant to all metal ion-conducting SEs with parent metal electrodes.<sup>35-39</sup>

### 2.1.1 Effect of the Time Scale on the Interplay of Constriction and Grain Boundary Characteristics

We start studying the influence of the interplay of the time scales of various microscopic or mesoscopic transport processes on the macroscopic impedance response of the system. For this purpose, two case studies were performed that differ in the material parameters of the pores and the grain boundaries ( $\tilde{C}_{\text{Pore}}$  and  $\varepsilon_{\text{GB}}$ , see Table 1) to ensure that the order of the time constants is either  $\tau_{\text{Bulk}} < \tau_{\text{GB}} < \tau_{\text{Cstr}}$  (case 1) or  $\tau_{\text{Bulk}} < \tau_{\text{Cstr}} < \tau_{\text{GB}}$  (case 2) independent of the contact area  $A_{\text{contact}}$ . As a result, Figure 3 a) and b) depict the macroscopic grain boundary fit parameters  $R_{\text{GB}}$  and  $C_{\text{GB}}$  as function of relative contact area, respectively.

The order of the time constants in case 1 ( $\tau_{\text{Bulk}} < \tau_{\text{GB}} < \tau_{\text{Cstr}}$ ) indicates that the pores at the interface are dielectrically conductive for frequencies around  $1/\tau_{\text{GB}}$ . In this frequency range, the electrode area actively contributing to the transport is the full SE surface area  $A_{\text{SE}}$ , i.e., there is no constriction present at the WE/SE interface. Thus, the current paths through the SE are quasi-1D and all the volume of the SE contributes to the transport as indicated by the green arrows in the upper part of Figure 3 a). This holds true regardless of the pore fraction at the interface. Therefore, the macroscopic transport quantities  $R_{\text{GB}}$  and  $C_{\text{GB}}$  are independent of the contact area  $A_{\text{contact}}$  as depicted in the lower part of Figure 3 a). Such a behavior is observed experimentally, e.g., during the dissolution (stripping) or deposition (plating) of the lithium metal anode with LLZO as SE.<sup>15, 40-41</sup>

The transport behavior is different when the order of the time constants of constriction and GB is reversed in case 2, i.e.,  $\tau_{\text{Cstr}} < \tau_{\text{GB}}$ , as can be seen in Figure 3 b). In this case, the GB signal lies in a frequency range where dynamic constriction is present at the interface, i.e., the pores are insulating. As a consequence, the sample volume of the SE pervaded by the current lines strongly depends on the contact area. In particular, only the grain boundary volume (i.e., area and thickness or transport length) pervaded by the current lines is reflected in the macroscopic parameters  $R_{\text{GB}}$  and  $C_{\text{GB}}$ . The resistance  $R_{\text{GB}}$  increases with decreasing contact area, as the volume of the SE effectively contributing to the transport is reduced in the constriction region. Similarly, the capacitance  $C_{\text{GB}}$  decreases with  $A_{\text{contact}}$ , since the effective area of the grain boundaries contributing to the transport is reduced, as shown in the upper part of Figure 3 b). In this context, it is important to note that the variation of the macroscopic GB parameters ( $R_{\text{GB}}$ ,  $C_{\text{GB}}$ ) with  $A_{\text{contact}}$  is due to the variation of the transport geometry and not associated with a change of the underlying microscopic transport quantities ( $\sigma_{\text{GB}}$ ,  $\varepsilon_{\text{GB}}$ ), which were kept constant in the corresponding computations.

Interestingly, the time constants derived from the (constant/varying) macroscopic fit parameters  $\tau_{\text{GB}} = R_{\text{GB}} \cdot C_{\text{GB}}$  are (almost) preserved in both series of computations. This finding is related to the fact that the transport through the SE can be approximately regarded as a parallel connection of different

serial transport paths. All those have in common that they contain shares of bulk and GB transport from both a local and macroscopic perspective. In this case, the initial phase information of the individual microscopic transport processes can be deconvoluted from the total impedance  $Z(f)$  as demonstrated in Equation S5 in the Supporting Information. This only applies to a symmetric arrangement where bulk and GB transport occur in each path (i.e., at least one grain boundary has to be crossed along each transport path). The theoretical consideration also highlights the presence of structural impedance contributions with mixed phase information. Apparently, the neglect of these contributions in 1D equivalent circuit analyses influences the derived macroscopic transport quantities ( $R_i$ ,  $C_i$ ) and thus the derived time constants  $\tau_i$ .<sup>10</sup> This is the reason for the slight deviations of the calculated  $\tau_{GB}$  from the microscopic parameter in the computations depicted in Figure 3 b).

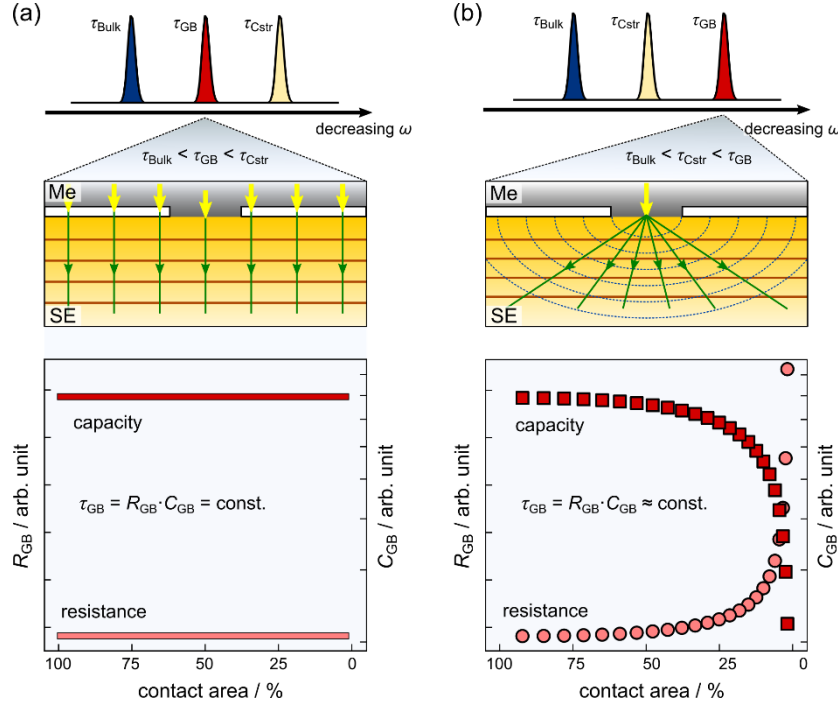


Figure 3. *Interplay of dynamic constriction with GB transport in the SE. Constriction at the interface influences all impedance contributions with lower characteristic frequencies than its own. (a) The pores at the interface have no impact on the macroscopic impedance contribution of GBs ( $R_{GB}$ ,  $C_{GB}$ ). In the frequency range around  $1/\tau_{GB}$ , the transport paths through the system (green arrows) are independent of the pore fraction at the interface. (b) The transport paths through the structure, the GB volume contributing to the transport, and thus the transport parameters ( $R_{GB}$ ,  $C_{GB}$ ) depend on the contact area between electrode and SE, if constriction occurs at higher characteristic frequencies than GB transport.*

### 2.1.2 Effect of the Microscopic Transport Parameters on the Constriction Characteristics

We will now turn to the effect of variations of microscopic bulk or GB transport quantities ( $\sigma_i$ ,  $\varepsilon_i$ ) on the derived constriction parameters ( $R_{Cstr}$ ,  $C_{Cstr}$ ) extracted from the computed impedance spectra with the help of the 1D-FM. For this purpose, we analyzed series of 3D computations in which we systematically varied the contact area at the WE/SE interface. In each series, we deliberately changed only one of the four microscopic transport parameters of the SE to study its qualitative effect on the impedance spectra.

Figure 4 shows the dependence of the constriction characteristics on the conductivities  $\sigma_i$  of a) bulk and b) GB transport. The overlapping symbols in the central graphs indicate that the constriction capacitance  $C_{\text{Cstr}}$  is not affected by a variation of the two SE related conductivities. In contrast, the constriction resistance  $R_{\text{Cstr}}$  increases for smaller conductivities  $\sigma_i$ . This is related to the non-local origin of this resistance. The potential distribution within the SE as well as the penetration depth into the SE and the size of the constriction region are functions of the conductivities  $\sigma_i$ . Therefore, the resistance  $R_{\text{Cstr}}$  can be considered a weighted linear combination of the individual microscopic transport processes in the system, i.e.,  $R_{\text{Cstr}} = \sum_i \alpha_i \cdot 1/\sigma_i$ . Here, the weighting factors  $\alpha_i$  depend on the potential distribution within the SE. This in turn is affected by the interface morphology, the structural composition of the constriction region (e.g., the number of grain boundaries near the interface, the effective contact area, the distribution of pores, etc.) and the characteristic time scales of individual transport processes occurring in the sample. The latter dependence is related to the fact that transport processes with a larger time constant than that of constriction are dielectrically shorted in the vicinity of  $1/\tau_{\text{Cstr}}$ , and, thus, have no (major) impact on the potential distribution and the size of the constriction region in the system.

The spatially weighted averaging of the different microscopic transport processes at the WE/SE interface and within the SE contributing to the macroscopic quantities  $R_{\text{Cstr}}$  and  $C_{\text{Cstr}}$  derived by fitting with 1D-FM are also the cause of the dependence of  $\tau_{\text{Cstr}}$  on contact area. The variation of  $A_{\text{contact}}$  affects the weights assigned to the contributing microscopic processes which typically exhibit different characteristic frequencies. Another interesting implication of the non-locality of the constriction effect is that the activation energy  $E_{a, \text{Cstr}}$  of the constriction resistance is an average of the activation energies  $E_{a, i}$  of the microscopic transport processes involved.

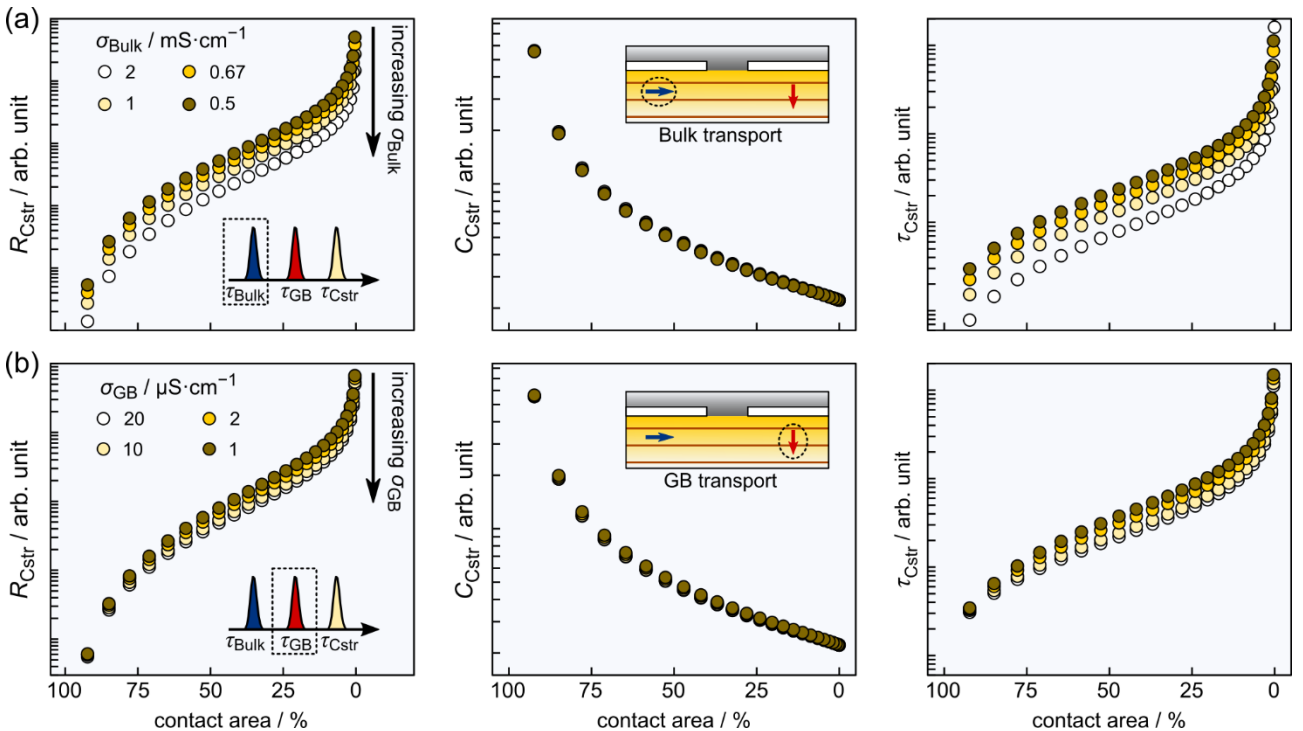


Figure 4. Dependence of the constriction behavior ( $R_{\text{Cstr}}$ ,  $C_{\text{Cstr}}$ ,  $\tau_{\text{Cstr}}$ ) on the conductivity of (a) bulk transport and (b) transport across GBs within the SE. The constriction resistance  $R_{\text{Cstr}}$  is only affected by transport processes with smaller time constant than its own ( $\tau_i < \tau_{\text{Cstr}}$ ), since these are electrically conductive around  $\tau_{\text{Cstr}}$  and thus influence the potential distribution and the size of the constriction region within the system. The constriction capacitance  $C_{\text{Cstr}}$  is unaffected in each case.

In contrast to the conductivities, the permittivities  $\varepsilon_i$  of bulk and GB transport processes within the SE neither affect the constriction resistance  $R_{\text{Cstr}}$  nor the constriction capacitance  $C_{\text{Cstr}}$  (not graphically depicted). This finding is independent of the order of time constants in the system. The independence of the constriction capacitance from the microscopic SE transport parameters is somewhat expected, since  $C_{\text{Cstr}}$  is mainly related to the pore capacitance and therefore to the interfacial properties, e.g., morphology, pore depth distribution, and pore permittivity.<sup>19</sup>

## 2.2 Effect of the Interface Characteristics on the Constriction Effect

Finally, we focus on the impact of the interface properties on the impedance, i.e., those of the non-ideal WE/SE interface and those of the ideal CE. We initially assume that the additional CT step at the ideal CE can be captured by our 1D-FM, since the interfacial contribution at the non-ideal WE/SE contact was separated into a CT and a constriction part. For the sake of simplicity and without loss of generality, the GBs within the SE are assumed to be highly conductive ( $Z_{\text{GB}} = 0$ ) in the following. Again, we will first consider the effect of the order of the characteristic time scales on the charge transfer characteristics ( $R_{\text{CT}}$ ,  $C_{\text{CT}}$ ) derived by 1D fitting approach and then discuss the impact of the variation of the microscopic interface transport parameters ( $R_{\text{Pol}}$ ,  $C_{\text{DL}}$ ) on the macroscopic constriction fitting parameters ( $R_{\text{Cstr}}$ ,  $C_{\text{Cstr}}$ ). The latter dependence is of particular interest, since many electrode/SE interfaces are not thermodynamically or kinetically stable, other than the Li/LLZO interface.<sup>39, 42-45</sup>

### 2.2.1 Effect of the Time Scale on the Interplay of Constriction and Charge Transfer Characteristics

Again, two extreme cases are considered where the material parameters of the pores and the charge transfer ( $\tilde{C}_{\text{Pore}}$  and  $C_{\text{DL}}$ , see Table 1) are chosen such that the order of time constants  $\tau_{\text{Bulk}} < \tau_{\text{CT}} < \tau_{\text{Cstr}}$  (case 1) and  $\tau_{\text{Bulk}} < \tau_{\text{Cstr}} < \tau_{\text{CT}}$  (case 2) is maintained independent of  $A_{\text{contact}}$ . Figure 5 a) and b) show the derived macroscopic CT quantities  $R_{\text{CT}}$  and  $C_{\text{CT}}$  as a function of the contact area for case 1 and 2, respectively.

In case 1 ( $\tau_{\text{Bulk}} < \tau_{\text{CT}} < \tau_{\text{Cstr}}$ ), the order of the time constants indicates that the CT steps at both interfaces, i.e., WE/SE and SE/CE interface, become electrically conductive in a frequency range where the pores at the WE/SE interface are dielectrically short-circuited. In an ideal scenario of negligible polarization resistance, the entire electrode area will actively contribute to the transport in the frequency range close to  $1/\tau_{\text{CT}}$  forming almost quasi-1D current paths from the non-ideal WE across the SE into the ideal CE as indicated in the upper part of Figure 5 a). The resistance  $R_{\text{CT}}$  will continuously decrease with decreasing contact area  $A_{\text{contact}}$  (i.e., increasing pore area), while the capacitance  $C_{\text{CT}}$  will increase as somewhat anticipated. In the limiting case of complete contact loss at the WE ( $A_{\text{contact}} = 0$  %), the resistance  $R_{\text{CT}}$  is half and the capacitance is twice the value compared to full contact ( $A_{\text{contact}} = 100$  %) as the CT step will exclusively occur at the ideal CE. The slight deviations from a linear behavior in the lower graph of Figure 5 a) are related to the nonzero polarization resistance, as will be discussed in detail in the next section.

The transport behavior is different, when the order of the time constants of CT and constriction is reversed, i.e.,  $\tau_{\text{Cstr}} < \tau_{\text{CT}}$ , as depicted in Figure 5 b). The CT effect will occur in a frequency range where the pores are electrically insulating so that the active electrode area will correspond to the physical contact area only. As a consequence, current spreading will occur leading to non-linear

changes of the CT quantities ( $R_{CT}$ ,  $C_{CT}$ ) as a function of the relative contact area  $A_{\text{contact}}$  at the WE/SE interface. The functional behavior in terms of curvature depicted in the lower graph of Figure 5 b) and its origin are comparable to that observed in Figure 3 b) for the interplay of grain boundaries and geometric constriction.

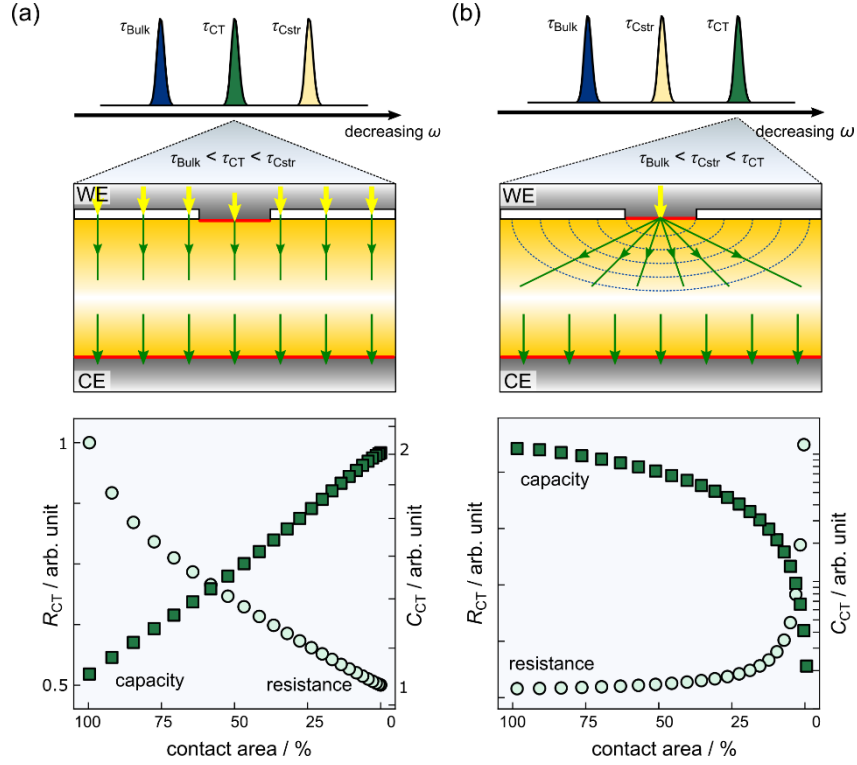


Figure 5. Interplay of dynamic constriction with charge transfer at the non-ideal WE/SE and ideal CE/SE interface. (a) Dielectrically shorted pores at the WE/SE interface ideally lead to quasi-1D pathways through the system (green arrows) around  $1/\tau_{CT}$ , regardless of the pore fraction at the interface. Thus, the macroscopic parameters ( $R_{CT}$ ,  $C_{CT}$ ) changes almost linearly with  $A_{\text{contact}}$ . (b) Electrically insulating pores around  $1/\tau_{CT}$  lead to current spreading near the WE/SE interface, which results in a strong dependence of ( $R_{CT}$ ,  $C_{CT}$ ) on the contact area between WE and SE.

### 2.2.2 Effect of the Microscopic Interface Parameters on the Constriction Characteristics

Now we turn to the impact of different microscopic interface transport quantities ( $R_{\text{Pol}}$ ,  $C_{\text{DL}}$ ) on the derived macroscopic constriction ( $R_{\text{Cstr}}$ ,  $C_{\text{Cstr}}$ ) and CT parameters ( $R_{CT}$ ,  $C_{CT}$ ) based on the fitting approach of the impedance spectra derived with the 3D network model with 1D-FM. For this purpose, we conducted a series of computations where we systematically varied the contact area at the WE/SE interface. We deliberately changed either the polarization resistance or the double-layer capacitance to identify corresponding trends.

The change of the double-layer capacitance  $C_{\text{DL}}$  does not affect the derived constriction parameters ( $R_{\text{Cstr}}$ ,  $C_{\text{Cstr}}$ ). This finding is similar to the variation of the bulk or GB permittivity  $\epsilon_i$  within the SE. The results are not graphically depicted. The situation is different when varying  $R_{\text{Pol}}$ . Figure 6 shows the dependence of the CT and constriction impedance ( $R_i$ ,  $C_i$ ,  $\tau_i$ ) on the magnitude of the polarization resistance. We chose the parameters such that the characteristic frequency of the microscopic CT migration process is larger than that of constriction ( $\tau_{CT} < \tau_{\text{Cstr}}$ ) independent of  $A_{\text{contact}}$ . Increasing the polarization resistance  $R_{\text{Pol}}$  leads to an increase of  $R_{CT}$  and  $R_{\text{Cstr}}$ . Interestingly, the respective

capacitances  $C_{CT}$  and  $C_{Cstr}$  also change, which was not the case when the conductivities within the SE were varied (see Figure 4). Larger polarization resistances lead to significant deviations from a linear relation of the CT parameters ( $R_{CT}$ ,  $C_{CT}$ ) in the intermediate  $A_{contact}$  range (cf. the dark green dots in Figure 6 a) and b)). Moreover, the slope and the sign of the curvature of the constriction capacitance  $C_{Cstr}$  vs  $A_{contact}$  changes when  $R_{Pol}$  is varied, while its qualitative behavior is unaffected ( $C_{Cstr} \rightarrow C_{Pore}^{1D-PM}$  for  $A_{contact} \rightarrow 0$ ). The more resistive the interfaces at the physical contact become, the more the curvature of  $C_{Cstr}$  vs  $A_{contact}$  approaches that of the macroscopic pore  $C_{Pore}^{1D-PM}$  vs  $A_{contact}$  (cf. Figure 2 d)).

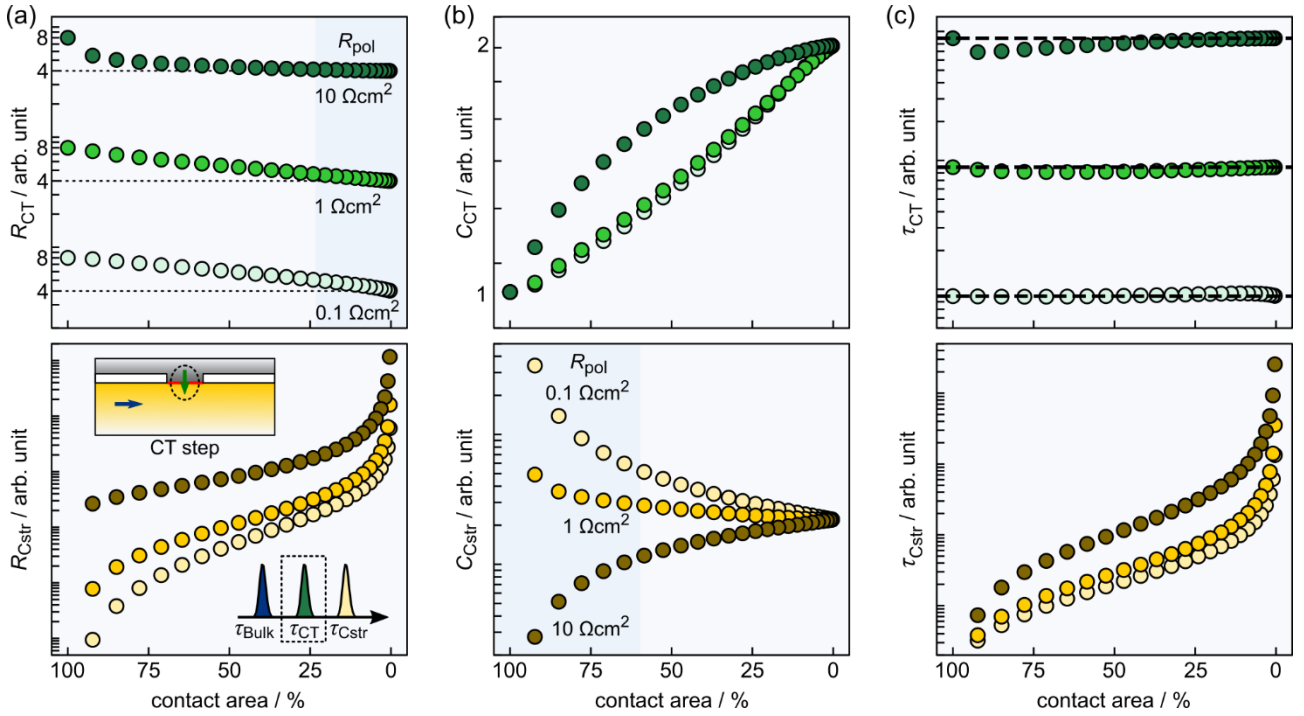


Figure 6. Dependence of the CT (top) and constriction (bottom) parameters, i.e. (a) the resistance  $R_i$ , (b) the capacitance  $C_i$  and (c) the time constant  $\tau_i$ , on the polarization resistance  $R_{Pol}$  at both electrode/SE interfaces. The size of  $R_{Pol}$  affects the energetically preferred current path at the WE interface, i.e., across the physical contact or through the pores, and thus the observed impedance behavior. The dashed horizontal lines in (c) indicate the microscopic (input) time constant of the CT step in the series of the 3D computations.

The observed behavior is related to the current path evolving at the interface. The arrangement of the time constants ( $\tau_{CT} < \tau_{Cstr}$ ) suggests that the CT steps at the interfaces become electrically conductive in a frequency range where the pores are dielectrically shortened. As a result, the ratio of the absolute values of pore impedance and the CT impedance (dominated by the polarization resistance) has a major effect on the amount of current flowing either across the physical WE/SE contact spots or across the pores as displacement current. The resulting spatial distribution of the total current dominates the overall impedance response of the system in this frequency range. The dependence of the current distribution at the interface and the associated transport across the SE on the polarization resistance is reflected, on the one hand, in the curvature of the CT fitting parameters ( $R_{CT}$ ,  $C_{CT}$ ) vs  $A_{contact}$  and, on the other hand, in the convergence behavior of the constriction capacitance  $C_{Cstr}$  vs  $A_{contact}$ . A smaller fraction of current flowing across the physical contact spot leads to a smaller CT resistance and a larger CT capacitance. This coincides with the fact that the larger the fraction of displacement current across the pores to the total current in the frequency range below  $1/\tau_{Cstr}$ , the

more the curvature of  $C_{\text{Cstr}}$  vs  $A_{\text{contact}}$  approaches that of the macroscopic pore capacity  $C_{\text{Pore}}^{\text{1D-PM}}$  vs  $A_{\text{contact}}$ . Thus, in case of high polarization resistance  $R_{\text{Pol}}$ , larger pore areas (or smaller contact area) would lead to an increased constriction capacity whereas smaller constriction capacitance would arise in case of negligible polarization resistances.

The qualitative behavior of  $R_{\text{Cstr}}$  and  $\tau_{\text{Cstr}}$  agrees with the conclusions drawn in the discussion of the impact of the microscopic transport quantities of the SE (see Figure 3). Both,  $R_{\text{Cstr}}$  and  $\tau_{\text{Cstr}}$  increase with increasing  $R_{\text{Pol}}$ . Interestingly, the time constant of the CT parameters  $\tau_{\text{CT}} = R_{\text{CT}} \cdot C_{\text{CT}}$  that should be independent of the contact area deviates for some records  $\tau_{\text{CT}}(A_{\text{contact}})$  from that of the microscopic (input) parameters as indicated by the dashed lines in Figure 6 c).

To clarify this issue, we compare in Figure 7 the impedance spectrum of a 3D electric network computation (black dots) with that of the corresponding 1D-FM fitting (red curve) and with the impedance of the modified 1D-PM (blue curve), where an additional  $RC$ -element connected in series was added to represent the CE. We assumed a polarization resistance of  $10 \Omega \cdot \text{cm}^2$  and a contact area of 78 % in this computation. For simplicity, the grain boundary impedance is set to zero and the SE is assumed to be bulk like. The Nyquist representation of the impedance spectra in Figure 7 a) visually consist of three well-separated semicircles. While the modified 1D-PM (blue) describes the bulk semicircle of the 3D electric network computation well, significant deviations occur for the interface impedances in the intermediate and low frequency range. Also, the fitted impedance curve according to 1D-FM cannot describe the impedance of the 3D computation in the intermediate frequency range.

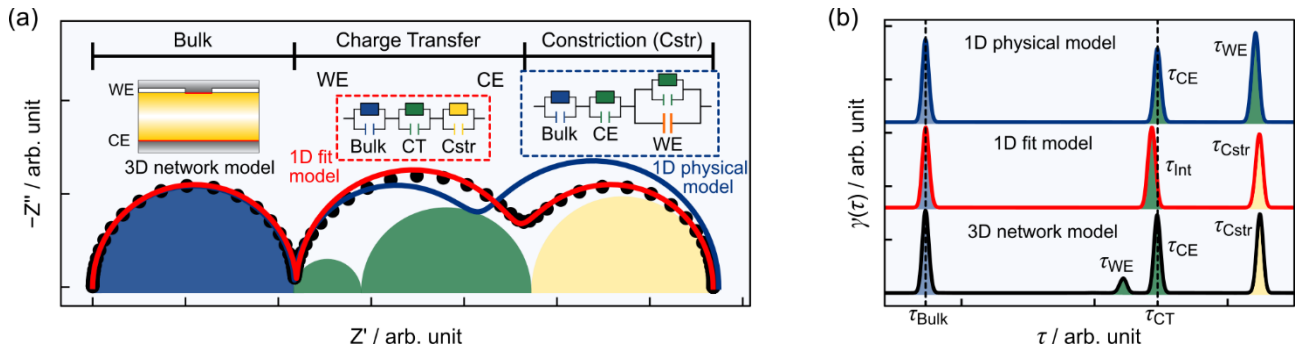


Figure 7. Comparison of the 3D electric network computation (black) with the simulated impedance of the 1D-FM (red) and with the calculated or predicted impedance of the modified 1D-PM (blue). Differences are clearly visible in both (a) the Nyquist plot and (b) the DRT representation of the individual impedances, especially with respect to the assignment of the single contributions. WE and CE must generally be considered separately when analyzing impedance data.

To study these deviations in more detail, we transfer the impedance curves  $Z(f)$  into the time domain by performing the individual DRT analyses, as shown in Figure 7 b). The DRT of the 3D network computation (black) consists of four signals originating from bulk transport in the SE, the non-ideal WE, the CT at the ideal CE and the constriction effect. While the time constants of bulk transport in the SE and CT at the CE are identical to the corresponding microscopic parameters in the computations, the time constant at the WE shifted towards smaller relaxation times compared to the microscopic  $\tau_{\text{CT}}$ . This is related to the multidimensional, non-serial transport behavior at the non-ideal WE/SE interface. The corresponding transport paths can be roughly regarded as the parallel connection of a pore capacitance and an  $R_{\text{CT}}C_{\text{CT}}$ -element. Since the two parallel paths are asymmetrical with respect to the transport processes involved (i.e., differ in terms of the microscopic transport mechanisms), the initial phase information of the microscopic CT step at the WE cannot be

deconvolved from the total impedance  $Z(f)$ , as demonstrated in the Supporting Information. Thus, the assumed pure CT impedance originating from the WE is actually a mixed signal composed in parts from the CT step and the pores. In contrast, the ideal CE/SE interface can be approximated by a single  $R_{CT}C_{CT}$ -element, i.e., the time constant of the microscopic CT step is preserved. This underlines the need for a decoupled consideration of the WE/SE and CE/SE interface in a macroscopic 1D picture.

The modified 1D-PM (blue) describes the WE and CE separately. While the behavior of bulk and the transport at the CE fit the 3D computation, major differences appear in the description of the non-ideal WE/SE interface. Neither can the constriction contribution be reproduced by 1D-PM, nor is the quantitative and qualitative behavior of the mixed WE signal of the 3D computation properly described, i.e., the shift direction of  $\tau_{WE}$  is incorrectly predicted and the amplitude and size of the shift are significantly overestimated. The 1D-FM (red), on the other hand, disregards a separate treatment of CT at the WE and CE. Both are described by the same single  $RC$ -element, leading to effective macroscopic transport parameters and a time constant different from the microscopic  $\tau_{CT}$ . The constriction contribution, in contrast, seems to be adequately captured. This implies that the fit model does not have enough degrees of freedom and needs to be extended to consider both interfaces separately.

### 2.3 Effect of Partially Overlapping Signals on the Impedance Analysis

In the sections above, only limiting cases have been discussed, i.e., the number of microscopic transport processes occurring within the system was reduced and the time constants of the individual macroscopic impedance contributions were well separated. This facilitated the assignment of different impedance contributions to microscopic transport processes as well as the analysis of the derived macroscopic fit parameters ( $R_i$ ,  $C_i$ ). Obviously, such clear separation does not always occur in experimental systems, e.g., several transport processes may take place in a similar frequency range causing (partially) overlapping impedance contributions. This impedes the analysis and interpretation of the impedance results. In particular, several microscopic transport processes even out of different layers of the sample structure may contribute to multiple macroscopic impedance contributions of the 1D fit equivalent circuit. As a consequence, there is not necessarily a one-to-one correspondence between assignment of the macroscopic transport quantities (e.g., to grain boundary or bulk processes in the SE or CT at the WE/SE interface) and the actual microscopic transport processes in these regions.

However, the qualitative trends derived in the respective case studies can also be observed for more realistic values of the individual time constants (i.e., overlapping impedance contributions). Typical experimental impedance data of reversible metal anodes consists of three (well-) separated contributions.<sup>15, 41</sup> These are usually assigned to bulk, GB and interface with decreasing frequency, respectively. The origin of “*the interface impedance*” is often not entirely clear in experiments. In case of lithium metal in contact with LLZO, it is reasonable that it results from geometric constriction rather than electric charge transfer.<sup>15, 17</sup> This indicates an ordering of time constants according to  $\tau_{Bulk} < \tau_{GB} < \tau_{Cstr}$ . In this sense, the qualitative results of the corresponding theoretical case study are comparable with the experimental observations, e.g., during the dissolution (stripping) or deposition (plating) of the lithium metal anode with LLZO as SE.<sup>15, 40-41</sup> The results for  $\tau_{Bulk} < \tau_{Cstr} < \tau_{GB}$  are also of great relevance, since the constriction effect strongly depends on the interface morphology, especially on the pore depth (distribution). Here, the effect of deep pores can occur at quite high

frequencies, which may lead to an influence on the macroscopic GB impedance contribution, e.g., due to an overlap of the corresponding impedance signals. In contrast, shallow pores cause a constriction at smaller frequencies similar to our computations.<sup>19</sup>

In many experimental situations a clear ordering of the time constants cannot be given, in particular, when both interface processes, CT and constriction, are present. The reason is that their frequency-dependent behavior is usually quite similar. As a consequence, corresponding experimental impedance spectra only exhibit one distorted interface contribution, which impedes a clear assignment of individual processes. An interpretation of the experimental results in terms of the case studies presented here, considering a clear ordering of the time constants is then not straightforward and a specific modelling is required.

## Summary and Conclusions

The following conclusions for the analysis of experimental impedance results with porous metal electrodes can be drawn from the modelling of situations accounting for constriction effect and CT effects at the interface between a metal electrode and a polycrystalline solid electrolyte. A few recommendations are formulated based on these conclusions:

- The impedance of the interface is generally composed of solid electrolyte interphase (SEI) and a CT contribution as well as a geometric constriction signal, when there is a non-ideal contact at the electrode/electrolyte interface. Dynamic constriction is a 3D effect that is related to the frequency-dependent change of the conduction behavior of pores or inclusions at interfaces. Its origin is on various length scales of the system ranging from mesoscopic to macroscopic.
- The time constant of the constriction signal  $\tau_{\text{Cstr}}$  has a major impact on the shape of the impedance spectrum and therefore on the interpretation of experimental data. It is a descriptor for the change between dielectric and insulating behavior of the pores or inclusions at the interface. The interplay between constriction and microscopic transport processes depends on the relative position of the individual time constants. Dynamic current constriction will exclusively affect the impedance contributions with larger time constant  $\tau_i$  than its own ( $\tau_{\text{Cstr}} < \tau_i$ ). The constriction contribution itself is only influenced by the transport processes with smaller time constant  $\tau_i$  than its own ( $\tau_i < \tau_{\text{Cstr}}$ ). The constriction contribution in the impedance may also overlap with several transport signals, compromising the interpretation and analysis of IS data, e.g., the derivation of microscopic transport parameters ( $\sigma_i, \varepsilon_i$ ).
- The geometric constriction resistance  $R_{\text{Cstr}}$  is of non-local origin and additionally increases the total resistance of a battery cell. It results from the frequency-dependent reduction of the SE volume contributing to the transport. It is composed of contributions of all transport processes that occur in the vicinity of the interface, i.e., the constriction region ( $R_{\text{Cstr}} = \sum_i \alpha_i \cdot 1/\sigma_i$ ). The weights  $\alpha_i$  of the individual contributions to  $R_{\text{Cstr}}$  depends severely on the interface morphology and the microstructure of the SE.
- The constriction capacitance  $C_{\text{Cstr}}$  is mainly affected by the pore characteristics at the interface and thus independent of the transport quantities of the SE. It is influenced by the morphology of the interface, e.g., the shape and depth of the pores as well as the distribution of the contact area, and the magnitude of the polarization resistance  $R_{\text{Pol}}$ .

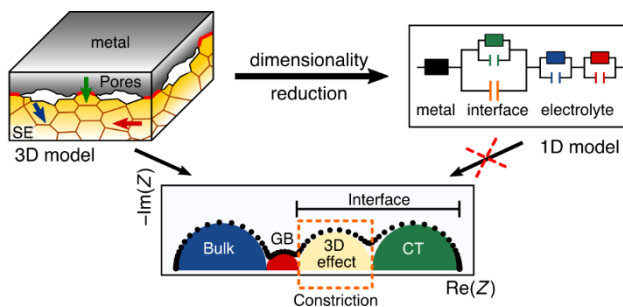
On the one hand, our study of the (dynamic) constriction effect underlines the power of the IS method, e.g., for the investigation of pore formation and the dynamics at the metal anode interface of solid-state batteries. On the other hand, it also shows the high potential for misinterpretations. IS data is usually analyzed by means of a macroscopic physical-based 1D equivalent circuit model, each component representing a transport process at the microscopic level. The computations using a 3D electric network model demonstrate that a non-physical 1D (fit) circuit model may represent a measured impedance spectrum well in some circumstances, but then the interpretation of the derived model parameters ( $R_i$ ,  $C_i$ ) is challenging. Physical motivated 1D equivalent circuit models, in contrast, cannot fully capture phenomena in real systems such as the geometric constriction effect. It is a misconception that there is a one-to-one correlation between macroscopic impedance response and microscopic electric transport processes.

Consequently, the analysis and interpretation of impedance data is challenging without an explicit theoretical model, which takes into account structural properties on the mesoscopic scale. Thus, careful correlations with the actual sample structure need to be established in order to avoid misinterpretations of the impedance analysis. In a forthcoming study, we will compare experimental data with our detailed 3D electric circuit model and simplified 1D representations, to highlight the practical relevance of our work.

## Acknowledgements

We acknowledge computational resources provided by the HPC Core Facility and the HRZ of the Justus-Liebig-University Giessen. We would like to thank MSc. Philipp Risius and Dr. Marcel Giar of HPC-Hessen, funded by the State Ministry of Higher Education, Research, and the Arts (HMWK), for programming advice. Financial support is provided by the DFG via the GRK (Research Training Group) 2204 “Substitute Materials for sustainable Energy Technologies”. J.J. and T.F. acknowledge funding by the German Federal Ministry of Education and Research (BMBF) of the LiSI project, grant identifier 03XP0224E. J.J. and S.B. acknowledges support by BMBF (Bundesministerium für Bildung und Forschung) within the Cluster of Competence FestBatt (projects 03XP0177A, 03XP0180, 03XP0433D).

## TOC Figure



## Keywords

reversible metal anode, interface morphology, pore formation, current constriction, impedance spectroscopy, solid-state battery, solid electrolyte, electric network model

## Supporting Information

Analytical consideration on the transformability of individual circuit elements.

## Competing Interests

The authors declare no competing interests.

## Data Availability

The data that support the findings of this study are available from the corresponding author upon reasonable request.

## References

1. Takeda, Y.; Yamamoto, O.; Imanishi, N., Lithium Dendrite Formation on a Lithium Metal Anode from Liquid, Polymer and Solid Electrolytes. *Electrochemistry* **2016**, *84* (4), 210-218.
2. Tarascon, J. M.; Armand, M., Issues and challenges facing rechargeable lithium batteries. In *Materials for Sustainable Energy*, Co-Published with Macmillan Publishers Ltd, UK: 2010; pp 171-179.
3. Xu, K., Nonaqueous Liquid Electrolytes for Lithium-Based Rechargeable Batteries. *Chem. Rev.* **2004**, *104* (10), 4303-4418.
4. McDowell, M. T.; Cortes, F. J. Q.; Thenuwara, A. C.; Lewis, J. A., Toward High-Capacity Battery Anode Materials: Chemistry and Mechanics Intertwined. *Chem. Mater.* **2020**, *32* (20), 8755-8771.
5. Janek, J.; Majoni, S., Investigation of Charge Transport Across the Ag|AgI-interface: (I) Occurrence of Periodic Phenomena During Anodic Dissolution of Silver. *Berichte der Bunsengesellschaft für physikalische Chemie* **1995**, *99* (1), 14-20.
6. Schmalzried, H.; Janek, J., Chemical kinetics of phase boundaries in solids. *Berichte der Bunsengesellschaft für physikalische Chemie* **1998**, *102* (2), 127-143.
7. Lewis, J. A.; Cortes, F. J. Q.; Liu, Y.; Miers, J. C.; Verma, A.; Vishnugopi, B. S.; Tippens, J.; Prakash, D.; Marchese, T. S.; Han, S. Y.; Lee, C.; Shetty, P. P.; Lee, H. W.; Shevchenko, P.; De Carlo, F.; Saldana, C.; Mukherjee, P. P.; McDowell, M. T., Linking void and interphase evolution to electrochemistry in solid-state batteries using operando X-ray tomography. *Nat Mater* **2021**, *20* (4), 503-510.
8. Vishnugopi, B. S.; Kazyak, E.; Lewis, J. A.; Nanda, J.; McDowell, M. T.; Dasgupta, N. P.; Mukherjee, P. P., Challenges and Opportunities for Fast Charging of Solid-State Lithium Metal Batteries. *ACS Energy Letters* **2021**, *6* (10), 3734-3749.
9. Lee, C.; Han, S. Y.; Lewis, J. A.; Shetty, P. P.; Yeh, D.; Liu, Y.; Klein, E.; Lee, H.-W.; McDowell, M. T., Stack Pressure Measurements to Probe the Evolution of the Lithium–Solid-State Electrolyte Interface. *ACS Energy Letters* **2021**, *6* (9), 3261-3269.

10. Eckhardt, J. K.; Burkhardt, S.; Zahnow, J.; Elm, M. T.; Janek, J.; Klar, P. J.; Heiliger, C., Understanding the Impact of Microstructure on Charge Transport in Polycrystalline Materials Through Impedance Modelling. *J. Electrochem. Soc.* **2021**, *168* (9), 090516.
11. Murugan, R.; Thangadurai, V.; Weppner, W., Fast Lithium Ion Conduction in Garnet-Type  $\text{Li}_7\text{La}_3\text{Zr}_2\text{O}_{12}$ . *Angew. Chem. Int. Ed.* **2007**, *46* (41), 7778-7781.
12. Zhu, Y.; Connell, J. G.; Tepavcevic, S.; Zapol, P.; Garcia-Mendez, R.; Taylor, N. J.; Sakamoto, J.; Ingram, B. J.; Curtiss, L. A.; Freeland, J. W.; Fong, D. D.; Markovic, N. M., Dopant-Dependent Stability of Garnet Solid Electrolyte Interfaces with Lithium Metal. *Advanced Energy Materials* **2019**, *9* (12), 1803440.
13. Connell, J. G.; Fuchs, T.; Hartmann, H.; Krauskopf, T.; Zhu, Y.; Sann, J.; Garcia-Mendez, R.; Sakamoto, J.; Tepavcevic, S.; Janek, J., Kinetic versus Thermodynamic Stability of LLZO in Contact with Lithium Metal. *Chem. Mater.* **2020**, *32* (23), 10207-10215.
14. Zhu, Y.; He, X.; Mo, Y., Origin of Outstanding Stability in the Lithium Solid Electrolyte Materials: Insights from Thermodynamic Analyses Based on First-Principles Calculations. *ACS Appl. Mater. Interfaces* **2015**, *7* (42), 23685-23693.
15. Krauskopf, T.; Hartmann, H.; Zeier, W. G.; Janek, J., Toward a Fundamental Understanding of the Lithium Metal Anode in Solid-State Batteries—An Electrochemo-Mechanical Study on the Garnet-Type Solid Electrolyte  $\text{Li}_{6.25}\text{Al}_{0.25}\text{La}_3\text{Zr}_2\text{O}_{12}$ . *ACS Appl. Mater. Interfaces* **2019**, *11* (15), 14463-14477.
16. Sharafi, A.; Kazyak, E.; Davis, A. L.; Yu, S.; Thompson, T.; Siegel, D. J.; Dasgupta, N. P.; Sakamoto, J., Surface Chemistry Mechanism of Ultra-Low Interfacial Resistance in the Solid-State Electrolyte  $\text{Li}_7\text{La}_3\text{Zr}_2\text{O}_{12}$ . *Chem. Mater.* **2017**, *29* (18), 7961-7968.
17. Gao, J.; Guo, X.; Li, Y.; Ma, Z.; Guo, X.; Li, H.; Zhu, Y.; Zhou, W., The Ab Initio Calculations on the Areal Specific Resistance of Li-Metal/ $\text{Li}_7\text{La}_3\text{Zr}_2\text{O}_{12}$  Interphase. *Advanced Theory and Simulations* **2019**, *2* (6), 1900028.
18. Cortes, F. J. Q.; Lewis, J. A.; Tippens, J.; Marchese, T. S.; McDowell, M. T., How Metallic Protection Layers Extend the Lifetime of NASICON-Based Solid-State Lithium Batteries. *J. Electrochem. Soc.* **2019**, *167* (5), 050502.
19. Eckhardt, J. K.; Klar, P. J.; Janek, J.; Heiliger, C., Interplay of Dynamic Constriction and Interface Morphology between Reversible Metal Anode and Solid Electrolyte in Solid State Batteries. *ACS Appl. Mater. Interfaces* **2022**, *14* (31), 35545-35554.
20. Fleig, J.; Maier, J., Finite element calculations of impedance effects at point contacts. *Electrochim. Acta* **1996**, *41* (7), 1003-1009.
21. Fleig, J.; Maier, J., Point contacts in solid state ionics: finite element calculations and local conductivity measurements. *Solid State Ionics* **1996**, *86-88*, 1351-1356.
22. Fleig, J.; Maier, J., The Influence of Laterally Inhomogeneous Contacts on the Impedance of Solid Materials: A Three-Dimensional Finite-Element Study. *J. Electroceram.* **1997**, *1* (1), 73-89.
23. Fleig, J.; Maier, J., Rough electrodes in solid and liquid electrochemistry: impact of morphology on the impedance. *Solid State Ionics* **1997**, *94* (1), 199-207.
24. Fleig, J.; Maier, J., The Influence of Current Constriction on the Impedance of Polarizable Electrodes: Application to Fuel Cell Electrodes. *J. Electrochem. Soc.* **1997**, *144* (11), L302-L305.
25. Fleig, J.; Maier, J., Finite-Element Calculations on the Impedance of Electroceramics with Highly Resistive Grain Boundaries: I, Laterally Inhomogeneous Grain Boundaries. *J. Am. Ceram. Soc.* **1999**, *82* (12), 3485-3493.
26. Boukamp, B., Electrochemical impedance spectroscopy in solid state ionics: recent advances. *Solid State Ionics* **2004**, *169* (1-4), 65-73.
27. Wan, T. H.; Saccoccio, M.; Chen, C.; Ciucci, F., Influence of the Discretization Methods on the Distribution of Relaxation Times Deconvolution: Implementing Radial Basis Functions with DRTtools. *Electrochim. Acta* **2015**, *184*, 483-499.
28. Rettenwander, D.; Welzl, A.; Cheng, L.; Fleig, J.; Musso, M.; Suard, E.; Doeff, M. M.; Redhammer, G. J.; Amthauer, G., Synthesis, Crystal Chemistry, and Electrochemical Properties

- of  $\text{Li}_{7-2x}\text{La}_3\text{Zr}_{2-x}\text{Mo}_x\text{O}_{12}$  ( $x = 0.1-0.4$ ): Stabilization of the Cubic Garnet Polymorph via Substitution of  $\text{Zr}^{4+}$  by  $\text{Mo}^{6+}$ . *Inorg. Chem.* **2015**, *54* (21), 10440-10449.
29. Loho, C.; Djenadic, R.; Bruns, M.; Clemens, O.; Hahn, H., Garnet-Type  $\text{Li}_7\text{La}_3\text{Zr}_2\text{O}_{12}$  Solid Electrolyte Thin Films Grown by  $\text{CO}_2$ -Laser Assisted CVD for All-Solid-State Batteries. *J. Electrochem. Soc.* **2016**, *164* (1), A6131-A6139.
  30. Tenhaeff, W. E.; Rangasamy, E.; Wang, Y.; Sokolov, A. P.; Wolfenstine, J.; Sakamoto, J.; Dudney, N. J., Resolving the Grain Boundary and Lattice Impedance of Hot-Pressed  $\text{Li}_7\text{La}_3\text{Zr}_2\text{O}_{12}$  Garnet Electrolytes. *ChemElectroChem* **2014**, *1* (2), 375-378.
  31. Beekmans, N. M.; Heyne, L., Correlation between impedance, microstructure and composition of calcia-stabilized zirconia. *Electrochim. Acta* **1976**, *21* (4), 303-310.
  32. van Dijk, T.; Burggraaf, A. J., Grain boundary effects on ionic conductivity in ceramic  $\text{Gd}_x\text{Zr}_{1-x}\text{O}_{2-(x/2)}$  solid solutions. *physica status solidi (a)* **1981**, *63* (1), 229-240.
  33. Verkerk, M. J.; Middelhuis, B. J.; Burggraaf, A. J., Effect of grain boundaries on the conductivity of high-purity  $\text{ZrO}_2\text{-Y}_2\text{O}_3$  ceramics. *Solid State Ionics* **1982**, *6* (2), 159-170.
  34. Fleig, J., Impedance Spectroscopy on Solids: The Limits of Serial Equivalent Circuit Models. *J. Electroceram.* **2004**, *13* (1), 637-644.
  35. Zhang, Z.; Wenzel, S.; Zhu, Y.; Sann, J.; Shen, L.; Yang, J.; Yao, X.; Hu, Y.-S.; Wolverton, C.; Li, H.; Chen, L.; Janek, J.,  $\text{Na}_3\text{Zr}_2\text{Si}_2\text{PO}_{12}$ : A Stable  $\text{Na}^+$ -Ion Solid Electrolyte for Solid-State Batteries. *ACS Applied Energy Materials* **2020**, *3* (8), 7427-7437.
  36. Wang, C.; Gao, J.; Gao, X.; Zhao, Y., Stabilizing the  $\text{Na}/\text{Na}_3\text{Zr}_2\text{Si}_2\text{PO}_{12}$  interface through intrinsic feature regulation of  $\text{Na}_3\text{Zr}_2\text{Si}_2\text{PO}_{12}$ . *Cell Reports Physical Science* **2021**, *2* (7), 100478.
  37. Krauskopf, T.; Richter, F. H.; Zeier, W. G.; Janek, J., Physicochemical Concepts of the Lithium Metal Anode in Solid-State Batteries. *Chem. Rev.* **2020**, *120* (15), 7745-7794.
  38. Krauskopf, T.; Mogwitz, B.; Hartmann, H.; Singh, D. K.; Zeier, W. G.; Janek, J., The Fast Charge Transfer Kinetics of the Lithium Metal Anode on the Garnet-Type Solid Electrolyte  $\text{Li}_6.25\text{Al}_0.25\text{La}_3\text{Zr}_2\text{O}_{12}$ . *Advanced Energy Materials* **2020**, *10* (27), 2000945.
  39. Bay, M.-C.; Wang, M.; Grissa, R.; Heinz, M. V. F.; Sakamoto, J.; Battaglia, C., Sodium Plating from  $\text{Na-}\beta''\text{-Alumina}$  Ceramics at Room Temperature, Paving the Way for Fast-Charging All-Solid-State Batteries. *Advanced Energy Materials* **2020**, *10* (3), 1902899.
  40. Wang, M. J.; Carmona, E.; Gupta, A.; Albertus, P.; Sakamoto, J., Enabling “lithium-free” manufacturing of pure lithium metal solid-state batteries through in situ plating. *Nature Communications* **2020**, *11* (1), 5201.
  41. Fuchs, T.; Haslam, C. G.; Moy, A. C.; Lerch, C.; Krauskopf, T.; Sakamoto, J.; Richter, F. H.; Janek, J., Increasing the Pressure-Free Stripping Capacity of the Lithium Metal Anode in Solid-State-Batteries by Carbon Nanotubes. *Advanced Energy Materials* **2022**, *n/a* (n/a), 2201125.
  42. Kasemchainan, J.; Zekoll, S.; Spencer Jolly, D.; Ning, Z.; Hartley, G. O.; Marrow, J.; Bruce, P. G., Critical stripping current leads to dendrite formation on plating in lithium anode solid electrolyte cells. *Nature Mater.* **2019**, *18* (10), 1105-1111.
  43. Schlenker, R.; Stępień, D.; Koch, P.; Hupfer, T.; Indris, S.; Roling, B.; Miß, V.; Fuchs, A.; Wilhelmi, M.; Ehrenberg, H., Understanding the Lifetime of Battery Cells Based on Solid-State  $\text{Li}_6\text{PS}_5\text{Cl}$  Electrolyte Paired with Lithium Metal Electrode. *ACS Appl. Mater. Interfaces* **2020**, *12* (17), 20012-20025.
  44. Spencer Jolly, D.; Ning, Z.; Hartley, G. O.; Liu, B.; Melvin, D. L. R.; Adamson, P.; Marrow, J.; Bruce, P. G., Temperature Dependence of Lithium Anode Voiding in Argyrodite Solid-State Batteries. *ACS Appl. Mater. Interfaces* **2021**, *13* (19), 22708-22716.
  45. Riegger, L. M.; Otto, S.-K.; Sadowski, M.; Jovanovic, S.; Kötz, O.; Harm, S.; Balzat, L. G.; Merz, S.; Burkhardt, S.; Richter, F. H.; Sann, J.; Eichel, R.-A.; Lotsch, B. V.; Granwehr, J.; Albe, K.; Janek, J., Instability of the  $\text{Li}_7\text{SiPS}_8$  Solid Electrolyte at the Lithium Metal Anode and Interphase Formation. *Chem. Mater.* **2022**, *34* (8), 3659-3669.